RESEARCH PAPER

Failure characteristics and development mechanism of fault rockburst in a deep TBM tunnel: a case study

Yu Zhang[1,2] · Xia-Ting Feng[1,2] · Zhibin Yao[1,2] · Wei Zhang[1,2] · Lei Hu[1,2] · Jun Wang[3] · Xinqiang Guo[3] · Wenjing Niu[1,2] · Yongwei Quan[3]

Abstract

An intense fault rockburst recently occurred in a deep tunnel excavated by tunnel boring machine in China, which was taken as a case to study the failure characteristics in detail. The temporal and spatial evolution of microseismic (MS) activity, the dynamic stress drop and the spatial distribution characteristics of rock fracture mechanism were analyzed. Stress-induced mechanism was studied using numerical simulation, and the development mechanism of the fault rockburst was revealed finally. The research results are as follows: (1) The development process of the fault rockburst is divided into six stages: calm stage, crack initiation stage, crack development stage, crack accumulation–slight fault dislocation stage, further crack accumulation stage and crack penetration–fault slip stage. (2) During the development of the fault rockburst, stress and energy accumulate in the deep of surrounding rock. When rockburst occurs, stress and energy are released in the shallow of the surrounding rock; at the same time, the dynamic stress drop increases significantly. MS energy is released intermittently during the development of fault rockburst. (3) Affected by the geological condition, the high in situ stress and the excavation unloading, horizontal shear slipping of the fault occurs, leading to fault rockburst. These research results can provide a reference for establishing the warning and mitigation methods of fault rockburst in deep TBM tunnels.

Keywords Development mechanism · Failure characteristics · Fault rockburst · Microseismic monitoring · TBM tunnel

1 Introduction

The fault rockburst is a common dynamic disaster in deep tunnels and metal mines, caused by shear slip of large fault structures under high stress. Fault rockburst poses a great hazard to construction and workers with a wider influence area and greatly destructive. For example, many fault rockbursts have occurred in the Witwatersrand gold mine and Carletonville gold mine in South Africa, and some rockbursts even have local magnitudes of 5.0, resulting in serious damage to the stope [5, 14]. An extremely intense fault rockburst occurred on November 28, 2009, in the drainage tunnel of the Jinping Hydropower Station in China. It caused seven workers dead, one person injury and a TBM buried completely, and the construction in the tunnel was shut down for half a year [36].

Scholars had conducted laboratory tests [11, 22], numerical simulations [1, 29] and field monitoring [16, 17] to study the development mechanism of the fault rockburst. In 1966, Brace and Byerlee [2] found a stick–slip phenomenon when studying rock friction; subsequently, stick–slip theory was proposed to describe the occurrence mechanism of shallow earthquakes. With the development of deep engineering, the fault rockburst attracted the attention of scholars, stick–slip theory was introduced to describe the occurrence mechanism of the fault rockburst. This theory has been verified by laboratory tests. Stress

✉ Xia-Ting Feng
  fengxiating@mail.neu.edu.cn

1 Key Laboratory of Ministry of Education on Safe Mining of Deep Metal Mines, Northeastern University, Shenyang 110819, China

2 Key Laboratory of Liaoning Province on Deep Engineering and Intelligent Technology, Northeastern University, Shenyang 110819, China

3 Xinjiang Erqisi River Basin Development and Construction Administration, Urumqi 830000, Xinjiang, China

drop and crack extension process were also observed via stick–slip testing [13, 21, 24, 32]. The relationship between rock friction and rockburst mechanisms has been studied through laboratory tests [18, 19, 28]. The characteristics of intermittent slipping during the evolution of fault slip were observed in the direct shear friction sliding test [30]. The super-shear stress theory [27] and shear slip theory [26] have been established to describe the fault dislocation mechanism. In addition, MS monitoring is the most effective technology to study the development process of rockbursts, which can be used to reveal the failure process of rock masses [7, 10, 38]. The evolution rule of sources during fault dislocation was clearly explained by the relationship between fault dislocation and stress in coal mines obtained through field MS monitoring [17, 31]. Zhang [39] studied the development mechanism of the fault slip rockburst in a deep tunnel excavated by drilling and blasting (D&B), showing that there were significant low-frequency characteristics when the fault rockburst occurred. Furthermore, some laboratory and field monitoring results showed that spectrum distributions mainly manifested low-frequency and high-amplitude spectra when fault rockburst occurred [15, 16, 34]. However, among the existing researches, few studies involved on the whole development process of the fault rockburst in deep hard rock tunnels, especially in TBM tunnel. The development mechanism of the fault rockburst is still limited to the level of theory and experience. Therefore, it is significant to study the development mechanism of the fault rockburst in deep TBM tunnels.

In this paper, an intense fault rockburst in a deep TBM tunnel in China is studied as a case. Based on a large amount of MS information and macro-failure characteristics, the development mechanism of the fault rockburst in a deep TBM tunnel was studied, which provides a theoretical basis for the warning and mitigation of the fault rockburst in deep tunnels. The research results are significant to the mitigation of fault rockbursts in deep TBM tunnels.

2 "2021.2.15" fault rockburst in a deep TBM tunnel

2.1 Engineering background

The geological conditions and layout of the tunnel are shown in Fig. 1. The lithology is mainly biotite granite. The in situ stress is highest in the horizontal direction. The maximum horizontal principal stress is approximately 36.0 MPa, and the angle between the direction of the maximum principal stress and the tunnel axis is approximately 65°, as shown in Fig. 1b. The tunnel was excavated by a TBM, with the total length of 20 km and maximum

burial depth of 712 m approximately. The trend of the tunnel is 169° with the diameter of 7 m. The cross section of the tunnel is shown in Fig. 1c. The equipment maintenance period is 9:00–14:00 every day, and the rest of the day is the excavation time. The overall rockburst risk is high in the tunnel, and rockburst occurs frequently during excavation.

On February 14–15, 2021, a fault rockburst occurred at K229 + 238 (Fig. 2). Buried depth of rockburst pit is approximately 692 m. A fault was developed in the rockburst area, rigid, straight, slightly open and partially filled with calcium. The dip angle of the fault is 25–30°, with dip direction of 345–350°, which is approximately consistent with the direction of the tunnel. The angle between the direction of maximum principal stress and the strike of fault is 21–26°. The lithology of the rockburst area is mainly biotite granite (Fig. 3a), with biotite K-feldspar granite distributed locally (Fig. 3b). Rock slice identification (Table 1) shows that some amphibole and biotite in biotite K-feldspar granite were metasomatized by chlorite and carbonate mineral aggregates, and slight alteration occurred (Fig. 4). According to the research results of Cheng [4] on the relationship between rock mineral composition and rock strength, the rock strength relationship is biotite granite > biotite K-feldspar granite. In addition, stress concentration area is formed in the interaction area between different lithologies and faults easily, so rockburst is more likely to occur in the interaction area between the biotite granite and fault. For the convenience of description, L is defined as the distance between the working face and the reference section A (K229 + 238) where the fault rockburst occurred (Fig. 5). A negative distance indicates that the working face has not been excavated to this section, and a positive distance indicates that it has passed through this section. D is defined as the tunnel diameter.

2.2 Occurrence process and failure characteristics of the "2021.2.15" fault rockburst

The occurrence process and failure characteristics of the "2021.2.15" fault rockburst are shown in Figs. 6, 7, 8, 9 and 10. At 9:00 on February 14, 2021, the working face was located at K229 + 233, $L = -5$ m, and no rockburst occurred during excavation. The local structural plane was supported by anchor bolts and reinforcing meshes (Figs. 7a, 8a). At 22:13 on February 14, the working face was located at K229 + 238, $L = 0$ m. The rockburst I occurred at 10–1 o'clock of tunnel section A, and the depth of the rockburst pit was approximately 0.6 m (Fig. 9a) which corresponds to a moderate rockburst. At this time, the rockburst pit was located inside the TBM shield and had not been exposed (Fig. 7b). The surrounding rock was still supported by

(a)

(b)　　　　　　　　　　　　　　　　(c)
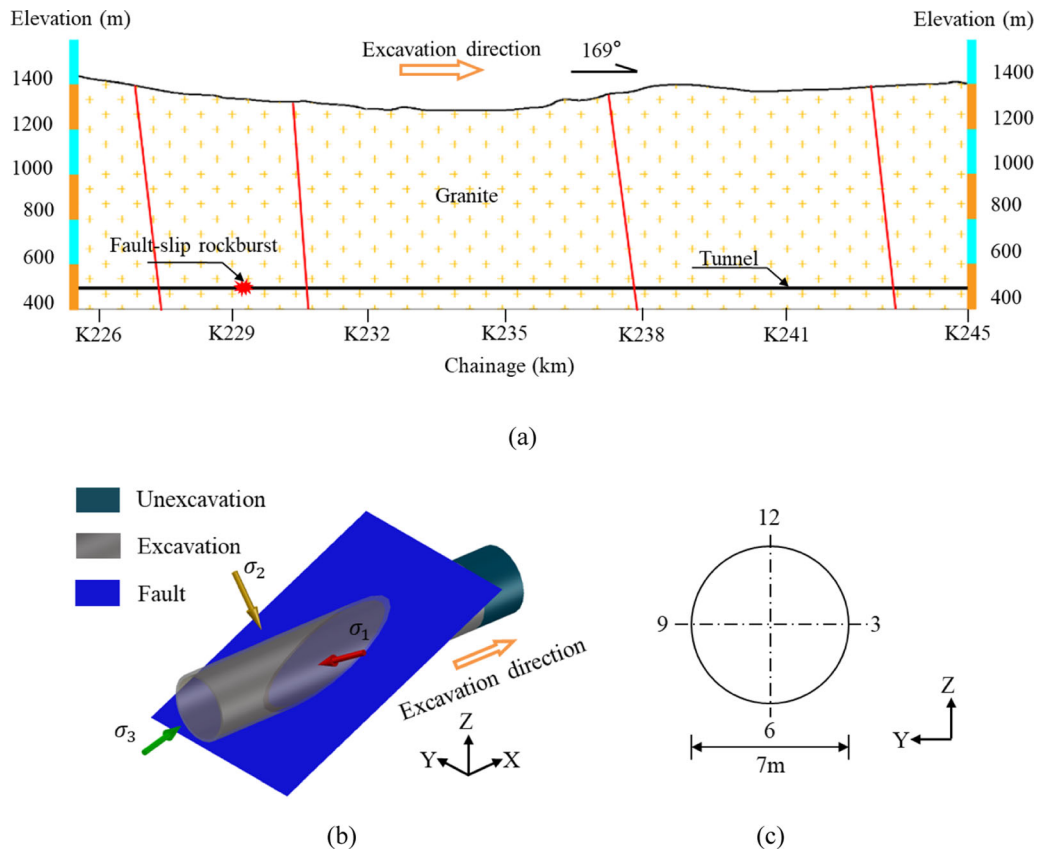
Fig. 1 The geological conditions and layout of the tunnel. **a** Geological profile of the tunnel. **b** Spatial relationship between the in situ stress and the tunnel axis. **c** cross section of tunnel
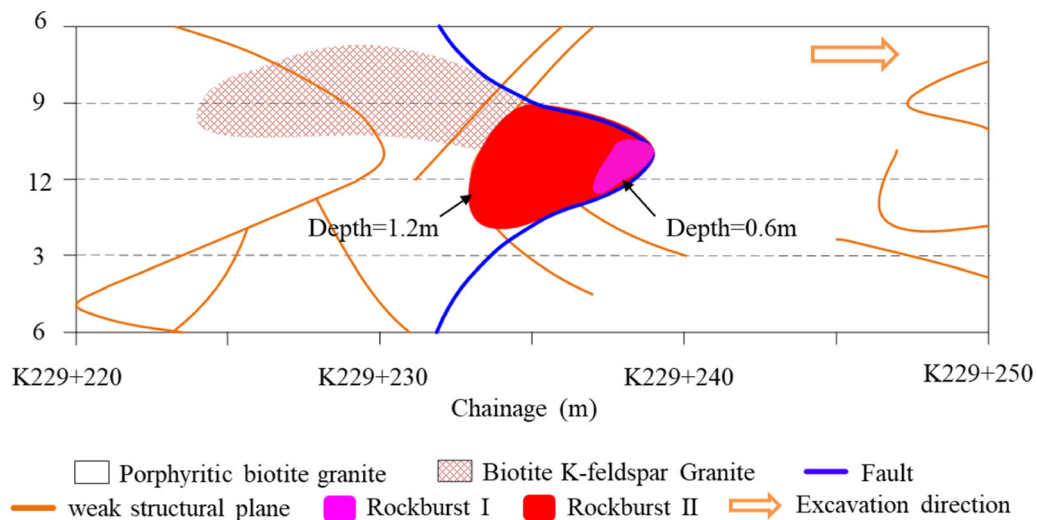
Fig. 2 Geological map of rock exposed at the tunnel surface in the fault rockburst area

anchor bolts and reinforcing meshes (Fig. 8b). Geological surveys showed that the fault had no significant dislocation after the occurrence of rockburst I (Fig. 8c). Then, surrounding rock was supported by the steel arch at K229 + 228 with the spacing between 0.9 and 1.2 m. At

9:00 on February 15, $L = 5$ m, the rockburst pit I was exposed (Fig. 8d) as the working face moved forward at K229 + 243 (Fig. 7c), where the steel arch was still used for surrounding rock support. At 18:58 on February 15, the working face located at K229 + 244.2 (Fig. 7d),

(a)

(b)
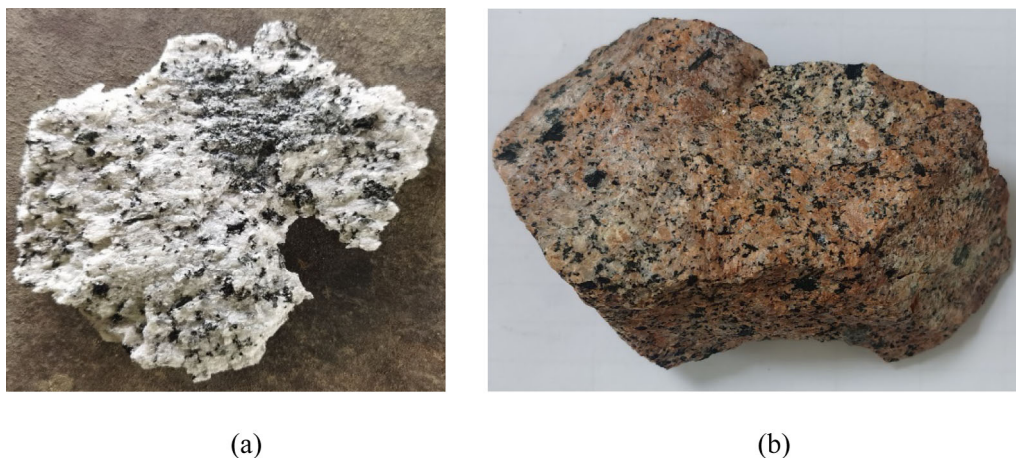
Fig. 3 Typical lithology in the fault rockburst area. **a** Biotite granite. **b** Biotite K-feldspar granite

Table 1 Mineral composition of the typical lithology based on rock slice identification

Lithology	Plagioclase (%)	k-feldspar (%)	Quartz (%)	Biotite (%)	Hornblende (%)
Biotite granite	55–60	10–15	20–25	1–2	2–3
Biotite K-feldspar granite	50–55	15–20	20–25	1–2	1–2
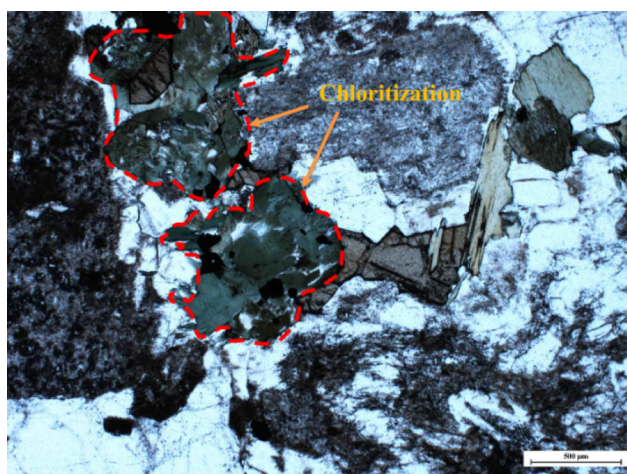
**Fig. 4** Local alteration of biotite K-feldspar granite
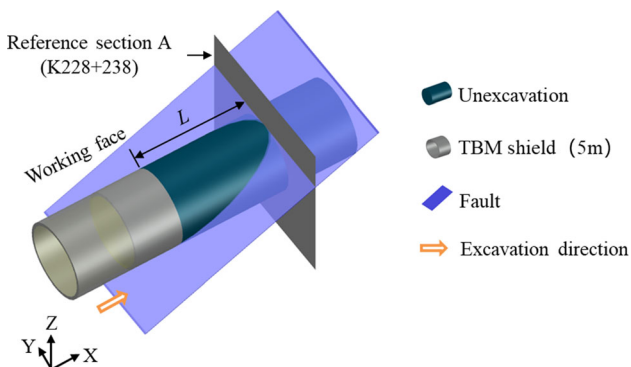
Fig. 5 The three-dimensional diagram of L

$L = 6.2$ m. Rockburst II occurred at 9–1 o'clock of the tunnel section (K229 + 237). The depth of the rockburst pit was approximately 1.2 m (Figs. 8e, 9b), which corresponds to an intense rockburst. According to the feedback of the staff, when rockburst II occurred, the muffled noise could be clearly heard approximately 4 km away from the rockburst area. Rockburst blocks were thick and massive plates that were not weathered (Fig. 9c). The fault had significant horizontal slipping, and the fault offset was approximately 10 cm (Figs. 8f, 10a). Gray–white rock powder can be clearly seen on the fault plane (Fig. 10b). At the same time, rockburst II caused serious deformation of the steel arch and reinforcing row within K229 + 230–239 (Fig. 10c, d), and the construction schedule was delayed for several days.

3 MS monitoring of the "2021.2.15" fault rockburst evolution processes

3.1 MS monitoring scheme

The SinoSeism (SSS) MS monitoring system [3] was used for MS monitoring during tunnel excavation. The main components of the system are shown in Fig. 11. The SSS system adopts the self-developed arrival time picker for MS rock fracturing [37], a sectional velocity model for MS source location identification in tunnels [6] and the identification of potential high-stress hazards in deep hard rock
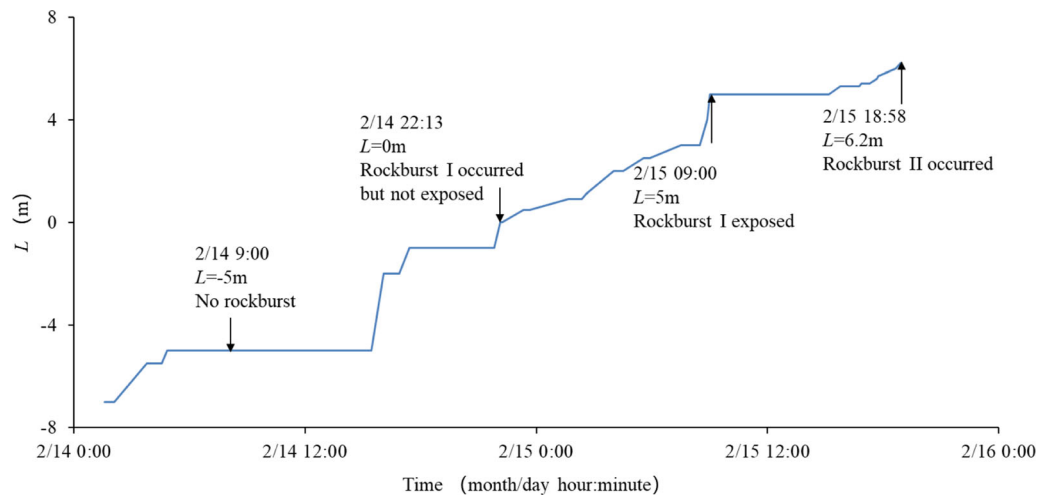
Fig. 6 Distance between the working face and reference section A during the occurrence of fault rockburst
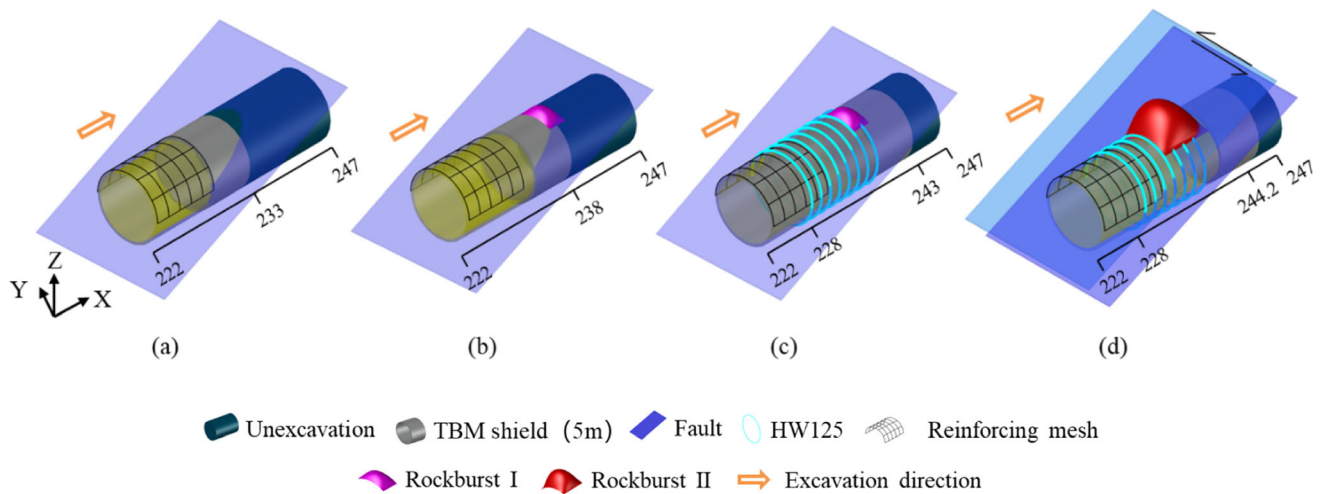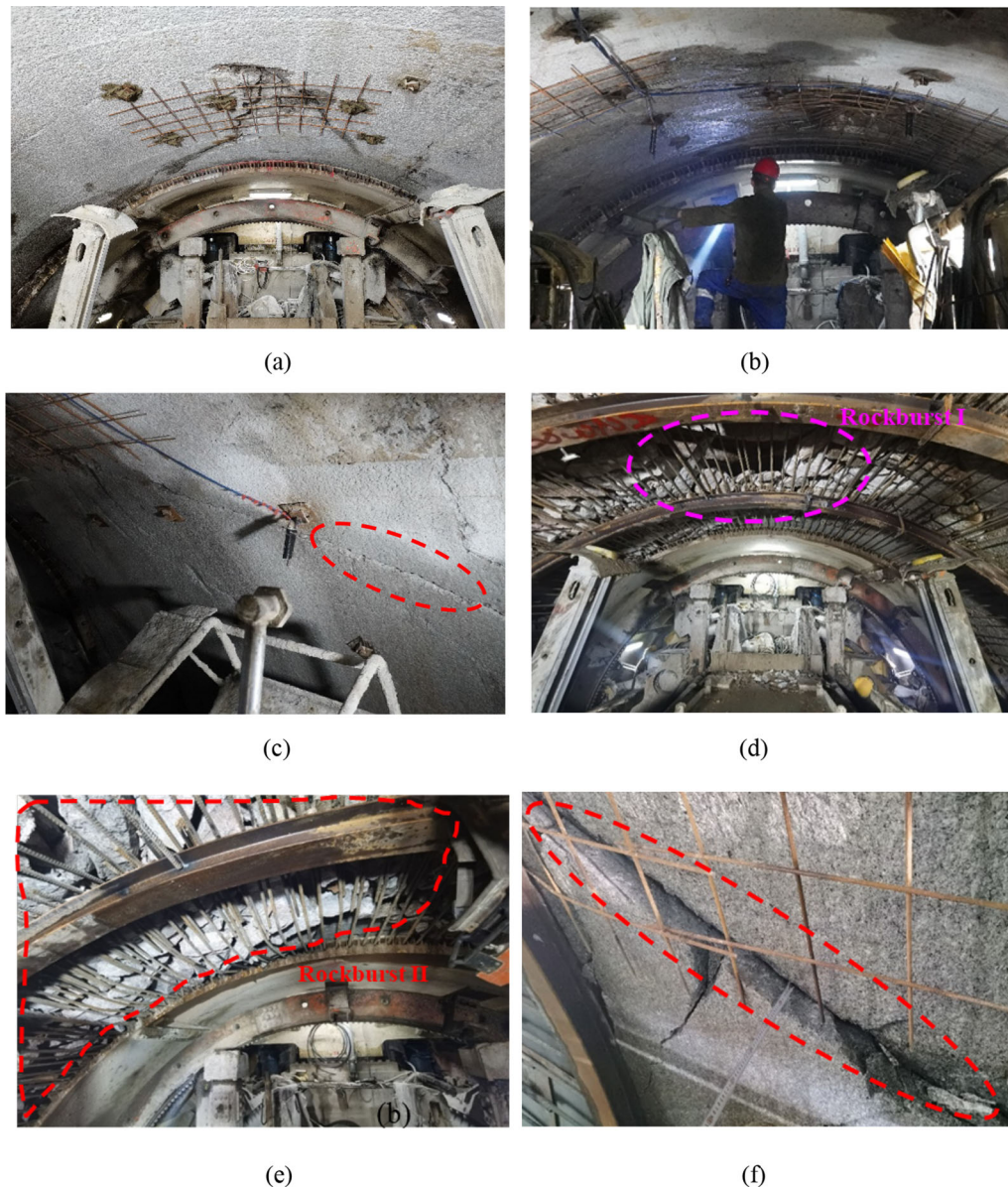

Fig. 7 Schematic diagram of the occurrence process of the intense fault rockburst. **a** At 9:00 on February 14, $L = -5$ m, no rockburst. **b** At 22:13 on February 14, $L = 0$ m, rockburst I occurred but not exposed. **c** At 09:00 on February 15, $L = 5$ m, rockburst pit I was exposed. **d** At 18:58 on February 15, $L = 6.2$ m, rockburst II occurred

tunnels [20] to carry out data analysis and disaster identification. The layout of the MS monitoring system is shown in Fig. 12. Two groups of sensors were used for MS monitoring, two rows (S1 and S2) were set up with four sensors installed in each row. The sensors have an approximate usable frequency range that varied from 10 to 2000 Hz, and the sensitivity is 80 V/ms^{-1}. S1(G1–G4) was installed approximately 5–10 m behind the working face. Two sensors were installed on both sides of the tunnel, respectively. S2(G5–G8) was installed approximately 15–20 m behind S1. After the working face moved forward 15–20 m, the S1 was recovered, the third group (S3) was installed 5–10 m behind the working face. S1 and S2 were moved forward alternately with the working face, which enabled real-time monitoring following TBM tunneling.

3.2 The temporal and spatial evolution characteristics of MS activity during the "2021.2.15" fault rockburst

The whole development and occurrence processes of the fault rockburst are recorded by MS monitoring system for the first time in a deep TBM tunnel. The MS events associated with the development and occurrence of fault rockburst were selected by the rockburst zone that was determined by the spatial distribution studies about the rockburst and the MS activity in TBM tunnels [40]. It showed by the field statistics that MS events associated with rockburst were mainly distributed within 35 m. Therefore, according to the spatial distribution and MS activity in TBM tunnels, the rockburst zone was selected as 10 m in front of working face and 25 m behind it. The

Fig. 8 Photographs of the support conditions and failure characteristics during the occurrence process of the intense fault rockburst. **a** At 9:00 on February 14, $L = -5$ m, the surrounding rock was supported by anchor bolts and reinforcing meshes. **b** At 22:13 on February 14, $L = 0$ m, the surrounding rock was still supported by anchor bolts and reinforcing meshes. **c** At 23:48 on February 14, the fault had no significant dislocation after the occurrence of rockburst I. **d** At 09:00 on February 15, $L = 5$ m, rockburst pit I is exposed **e** At 18:58 on February 15, $L = 6.2$ m, rockburst II occurred. **f** At 18:58 on February 15, the fault had significant horizontal slipping

spatial distribution characteristics of MS events during the "2021.2.15" fault rockburst are shown in Fig. 13. Each ball represents an MS event, the color of the spheres represents the occurrence time of the MS events, and the size represents the logarithm of the MS energy.

Figure 13a–e shows the spatial evolution characteristics of MS events when the working face gradually approached the reference section A. When $L = -20 \sim -15$ m, MS events were mainly distributed at 12 o'clock of the working face, and the logarithm of MS energy (LgE) was less than 3.0. There was only one MS event with LgE = 2.12 near

the fault, the potential rockburst area was hardly affected by the fault. When $L = -15 \sim -3$ m, MS events gradually accumulated in the potential rockburst area near the fault and were distributed along the fault. Some high-energy (LgE ≥ 3.0) events began to occur in the deep of the surrounding rock near the fault (approximately 10–15 m from the tunnel surface), and gradually developed to the shallow of the surrounding rock along the fault. This process showed that MS activity tended to be active near the fault. When $L = -3$–0 m, MS events accumulated and gathered at 9–12 o'clock in the tunnel section
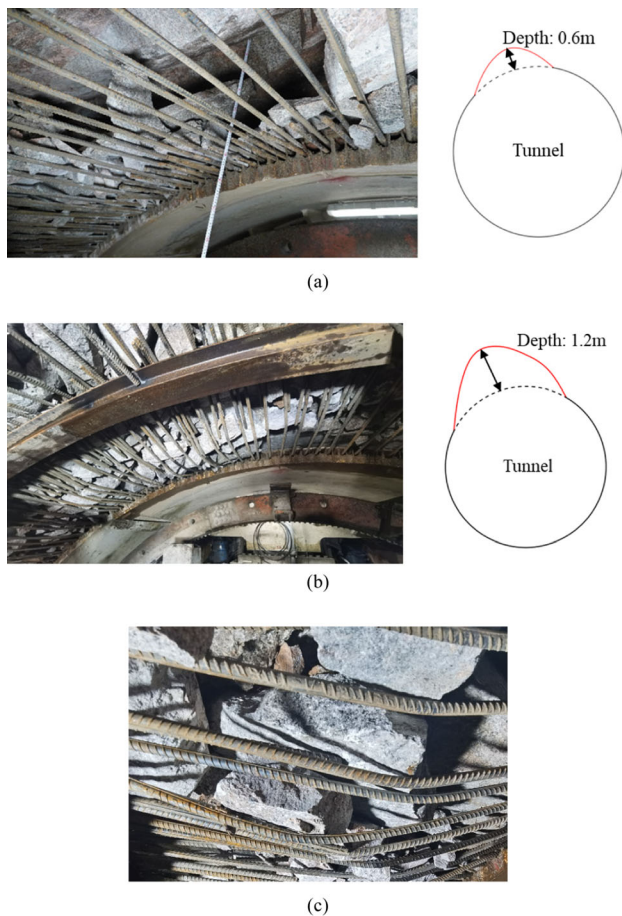
Fig. 9 Rockburst pits and rockburst blocks of the fault rockburst. **a** Site photograph of rockburst I and cross section of the rockburst pit I. **b** Site photograph of rockburst II and cross section of the rockburst pit II. **c** Rockburst blocks after rockburst II occurred

(K229 + 238), high-energy MS events were distributed in the shallow area of the surrounding rock along the fault (approximately 0–3 m from the tunnel surface). When $L = 0$ m, rockburst I occurred at 11–12 o'clock of the working face. When $L = -2D$, the fault area began to be affected, and MS activity tended to be active. According to the spatial distribution, MS events were mainly concentrated in the hanging wall of the fault at 9–12 o'clock and distributed along the fault.

Figure 13f–i shows the spatial evolution characteristics of MS events when the working face gradually moved away from the reference section A. When $L = 0–1.1$ m, MS events were mainly distributed at 9–12 o'clock of the tunnel section (K229 + 238) behind the working face, high-energy events were distributed along the fault at approximately 8–10 m from the tunnel surface, and low-energy events were distributed discretely. When $L = 1.1–5.5$ m, MS events gradually concentrated at 9–12 o'clock in the tunnel section (K229 + 238). At this time, many high-energy MS events were generated along the

fault plane and concentrated gradually. When $L = 5.5–6.2$ m, many high-energy MS events accumulated and were distributed approximately 5–7 m from the tunnel surface. Before rockburst II occurred, many high-energy events were continuously generated at 11 o'clock in the section, the greatest logarithm of MS energy observed was 5.3.

The distances between MS events with LgE $\geq$ 3.0 and the tunnel surface were recorded during the development of fault rockburst (Fig. 14). Figures 13 and 14 show that the high-energy events firstly occurred in the deep of the surrounding rock near the fault plane. With the excavation, MS events gradually developed from deep to shallow of the surrounding rock along the fault, finally, rockburst occurred, and the energy was released in the shallow of the surrounding rock.

The evolution of the energy of the MS events during the development of the fault rockburst is shown in Fig. 15, each MS event is a crack. According to the above laws and characteristics, when the working face approached the fault, MS activity gradually became active. When rockburst was about to occur, a large number of MS events with LgE $\geq$ 3.0 were generated in a short time, and the energy accumulated rapidly, which indicated that rockburst risk increased. After rockburst II occurred, MS activity gradually tended to be stable, low-energy events generated. Based on the above characteristics and Fig. 13, the failure process of the "2021.2.15" fault rockburst can be divided into six stages:

(I) Calm stage ($L = -20 \sim -15$ m): MS activity was relatively calm and dominated by low-energy events. The greatest number of MS events collected was 21. These MS events were distributed around the tunnel and close to the working face, and the greatest logarithm of MS energy observed was 2.12.

(II) Crack initiation stage ($L = -15 \sim -10$ m): MS activity began to be active, and the cumulative MS energy increased rapidly. MS events with LgE < 3.0 were 81.3%. MS events were gradually distributed along the fault. In this stage, 39 MS events were collected, and the greatest logarithm of MS energy observed was 3.13. This stage indicates that the fault began to be affected.

(III) Crack development stage ($L = -10 \sim -3$ m): MS activity continued to be active in this stage, the cumulative MS energy continued to increase, 24 MS events were collected, and the greatest logarithm of MS energy observed was 3.65. MS event developed from deep to shallow of the surrounding rock along the fault, and the energy of
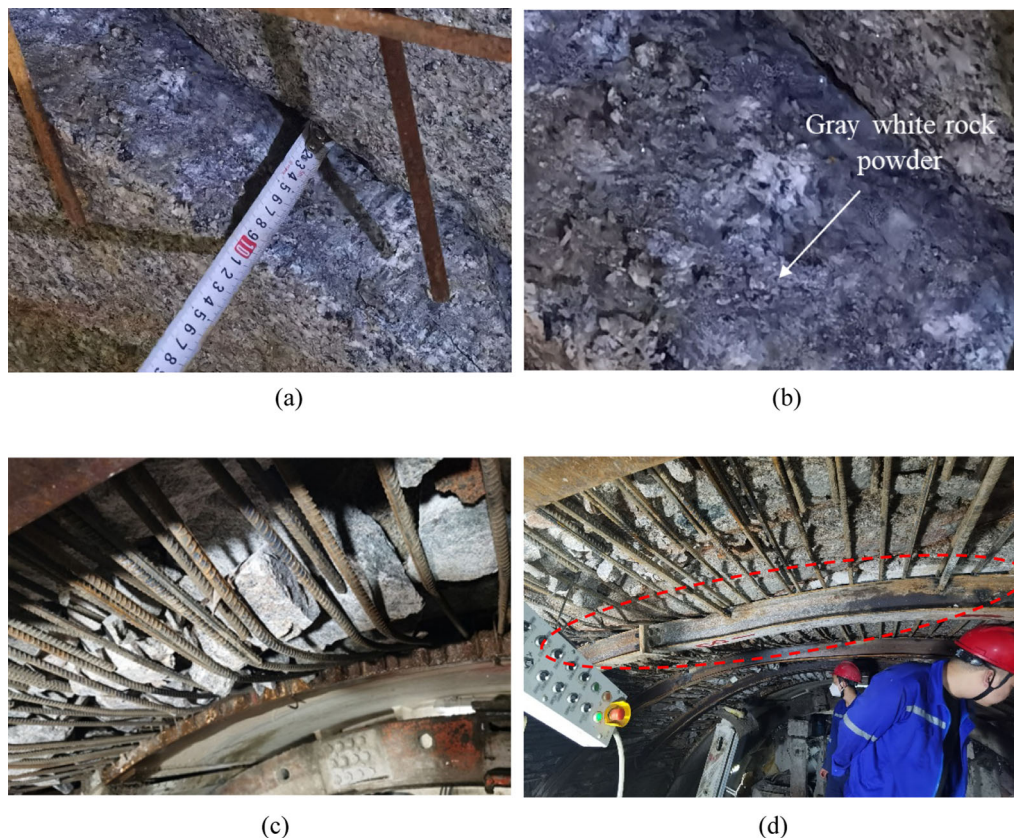
Fig. 10 Fault slip and support failure during the fault rockburst. **a** Fault slip distance. **b** Rock grains and gray–white rock powder. **c** Reinforcement row deformation. **d** Steel arch deformation
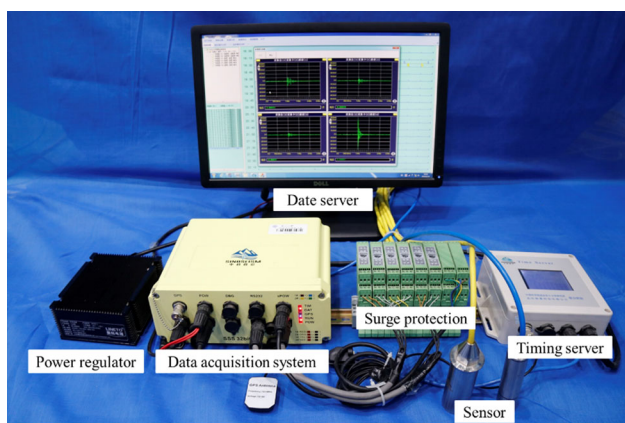
Fig. 11 The SSS MS monitoring system

the potential rockburst area was further concentrated.

(IV)   Crack accumulation–slight fault dislocation stage ($L = -3$–0 m): MS activity increased rapidly, 16 MS events were collected, and the greatest logarithm of MS energy observed was 4.58. The relatively active MS activity indicates that there was a high rockburst risk at this time.

(V)   Further crack accumulation stage ($L = 0$–5.5 m): MS activity continued to be active, and MS events occurred and concentrated continuously near the fault plane. A total of 31 MS events were collected, and the greatest logarithm of MS energy observed was 4.43. The energy was further concentrated in this stage.

(VI)   Crack penetration–fault slip stage ($L = 5.5$–6.2 m): the accumulated energy increased abruptly, and MS events were distributed along the fault. A total of 15 MS events were collected, and the greatest logarithm of MS energy observed was 5.3. The intense MS activity indicated that the rockburst with high intensity was about to occur in this stage.

3.3 Development of dynamic stress drop during the "2021.2.15" fault rockburst

The dynamic stress drop is the stress difference between prior- and post-fault slip, which represents the stress release on the fracture surface when the rock mass fractures [25]. The greater the dynamic stress drop, the more likely

(a)   (b)
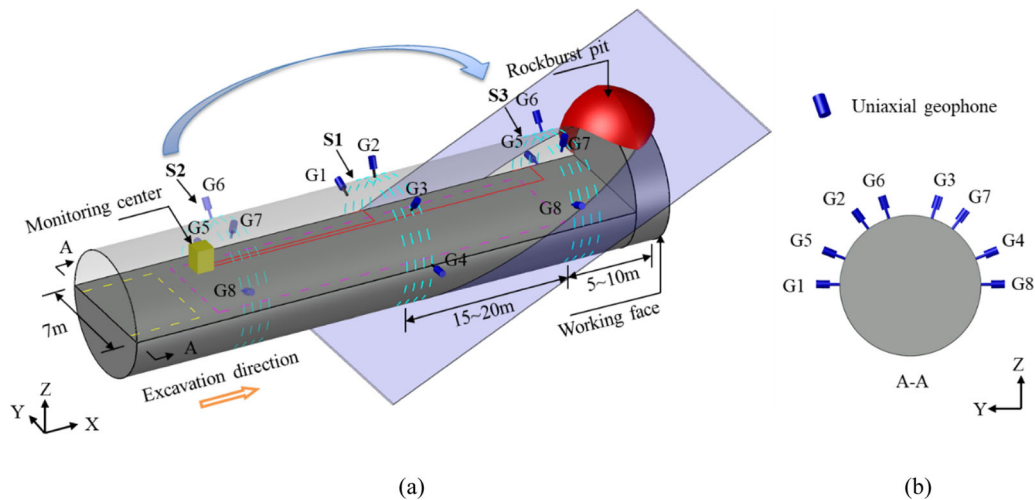
Fig. 12 Sketch of the layout of the MS monitoring system in the deep TBM tunnel. **a** Three-dimensional representation of the MS sensor array. **b** Arrangement of the MS sensors as viewed along the axis of the tunnel

severe shear instability is to occur [12]. According to the obtained MS information, the distribution and evolution characteristics of the dynamic stress drop are studied during the development of the "2021.2.15" fault rockburst, and the stress level in the fault area is analyzed, as shown in Fig. 16.

Figure 16a–e shows that the distribution of the dynamic stress drop when the working face gradually approached the reference section A. As shown in Figs. 16a–e and 17, when $L = -20 \sim -15$ m, $L = -15 \sim -10$ m, $L = -10 \sim -5$ m, $L = -5 \sim -3$ m and $L = -3 \sim 0$ m, the largest values of the dynamic stress drop were 0.89 MPa, 1.37 MPa, 1.77 MPa, 1.78 MPa and 3.51 MPa, respectively. When $L = -20 \sim -15$ m, the dynamic stress drop was at a low level, mainly concentrated in the shallow of the surrounding rock. When $L = -15 \sim -3$ m, the dynamic stress drop increased slowly near the hanging wall. With the decrease in L, the dynamic stress drop gradually developed to the shallow of the surrounding rock. When $L = -3{-}0$ m, the dynamic stress drop increased to 3.51 MPa rapidly, it was concentrated at 9–12 o'clock of the tunnel section (K229 + 238), which meant that the fault may have experienced slight dislocation. Finally, when $L = 0$ m, rockburst I occurred, and stress was released in the shallow of the surrounding rock.

Figure 16f–i shows the distribution of the dynamic stress drop when the working face gradually moves away from the reference section A. When $L = 0 \sim 1.1$ m, $L = 1.1{-}5$ m, $L = 5{-}5.5$ m and $L = 5.5{-}6.2$ m, the largest values of the dynamic stress drop are 1.95 MPa, 3.97 MPa, 1.35 MPa and 7.89 MPa. After rockburst I occurred, partial stress was released near the fault, but the high stress level was still maintained. When $L = 0{-}5.5$ m, the dynamic

stress drop continued to increase near the fault, it was concentrated in the hanging wall during the stress developed from deep to shallow of the surrounding rock near the fault. When $L = 5.5{-}6.2$ m, the dynamic stress drop sharply increased to 7.68 MPa and was concentrated in the shallow of the surrounding rock near the fault, resulting in rockburst II with a larger damage scale.

The above analysis shows that during the development of fault rockburst, the dynamic stress drop concentration area gradually developed from deep to shallow of the surrounding rock, stress was concentrated in the potential rockburst area. The dynamic stress drop increased abruptly before rockburst occurred, it means that shear slip was very likely to occur at this time.

4 The mechanism of the "2021.2.15" fault rockburst

4.1 Rock fracture mechanism during the "2021.2.15" fault rockburst

Studies have shown that the fracture type of rock microfractures is closely related to the time-domain characteristics of the waveform. Therefore, the fracture type is judged based on the P-wave development of the events [35]. The evolution and distribution of the fracture type during the development of the fault rockburst are shown in Fig. 18. The blue spheres represent tensile fractures, the red spheres represent shear fractures, and size represents the logarithm of the MS energy.

Figure 18a–e shows the spatial distribution of fracture type when the working face gradually approached the reference section A. When $L = -20 \sim -15$ m, the rock
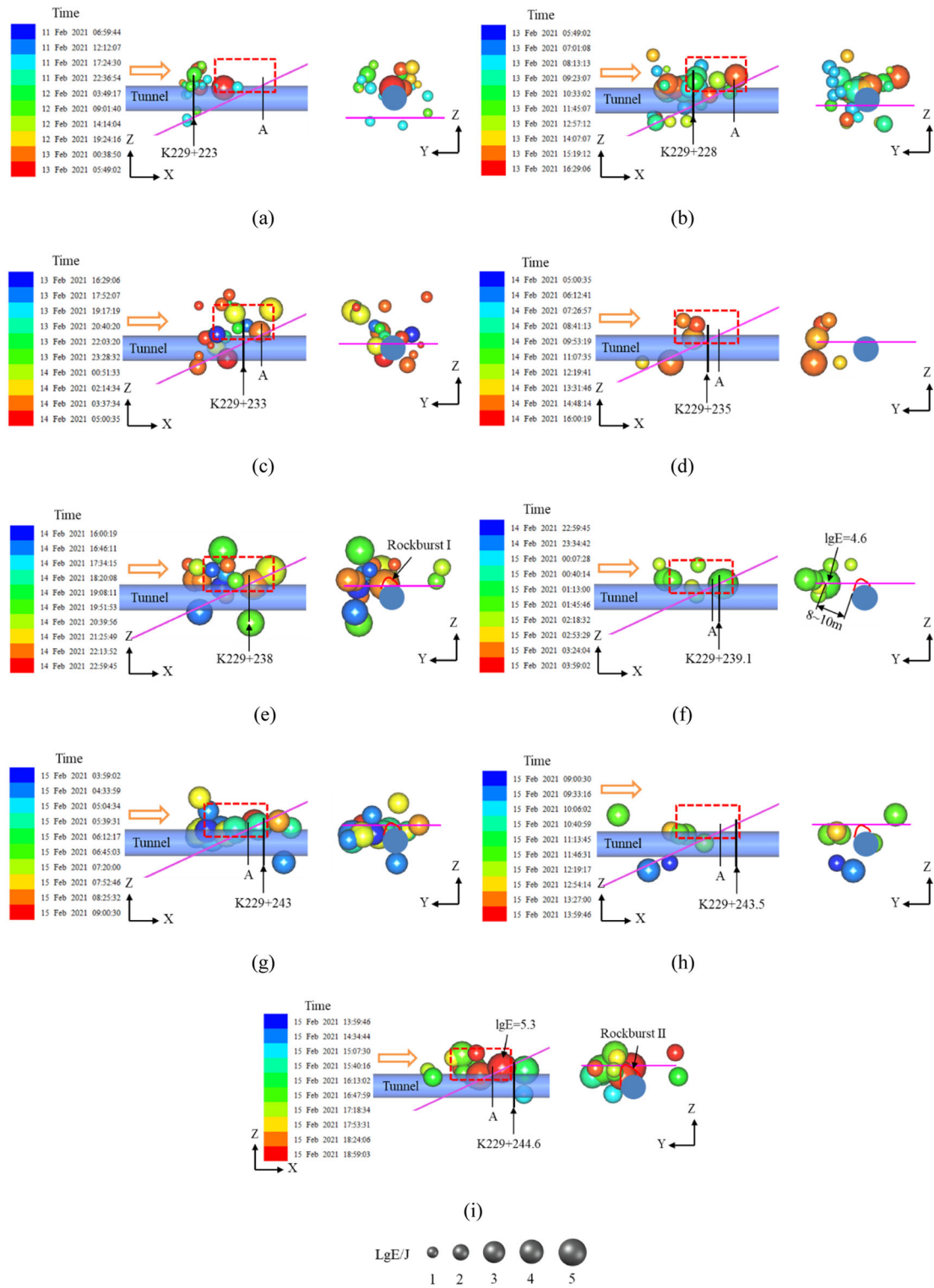
Fig. 13 Evolution of the distribution of the MS events during the development process of fault rockburst with different distance *L*. **a** *L* = − 20 ∼ − 15 m. **b** *L* = − 15 ∼ − 10 m. **c** *L* = − 10 ∼ − 5 m. **d** *L* = − 5 ∼ 3 m. **e** *L* = − 3 ∼ 0 m. **f** *L* = 0 ∼ 1.1 m. **g** *L* = 1.1 ∼ 5 m. **h** *L* = 5–5.5 m. **i** *L* = 5.5–6.2 m

fracture events were mainly tensile fractures and concentrated near the working face. When $L = -15 \sim -10$ m, tensile and shear fracture events occurred together, and some shear fracture events began to distribute along the fault plane. When $L = -10 \sim -3$ m, the proportion of shear fracture events increased, some shear fracture events were distributed along the fault, and sporadic tensile fracture events occurred near the fault plane in the deep of the surrounding rock. When $L = -3$–0 m, with the occurrence of rockburst I, a large number of high-energy shear fracture events were concentrated on the arch of the surrounding

rock near the fault, and some were distributed along the fault, which indicated that the fault had slight dislocation. The analysis shows that the rock fracture events were mainly tensile fractures during the development of rockburst. When the working face approaches the reference section A, the type of fracture event turns to the tensile and shear fractures gradually. When rockburst I occurred, the rock fracture events were mainly shear fractures.

Figure 18f–i shows the spatial evolution characteristics of MS events when the working face gradually moved away from the reference section A. When $L = 0$–1.1 m,
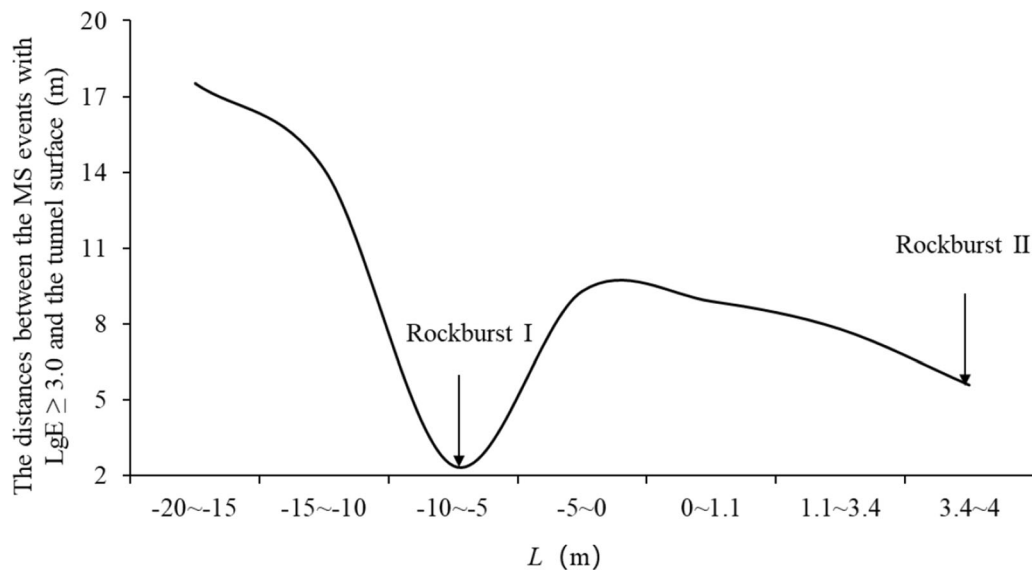

Fig. 14 The distances between the MS events with LgE $\geq$ 3.0 and the tunnel surface during the development process of the fault rockburst
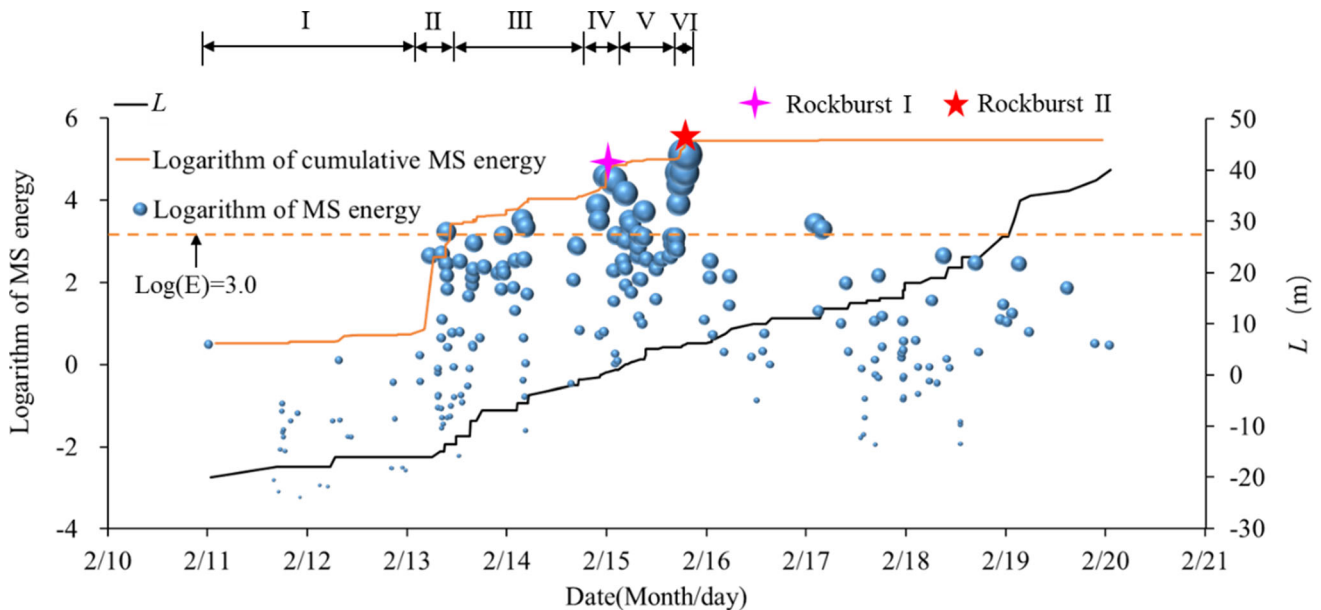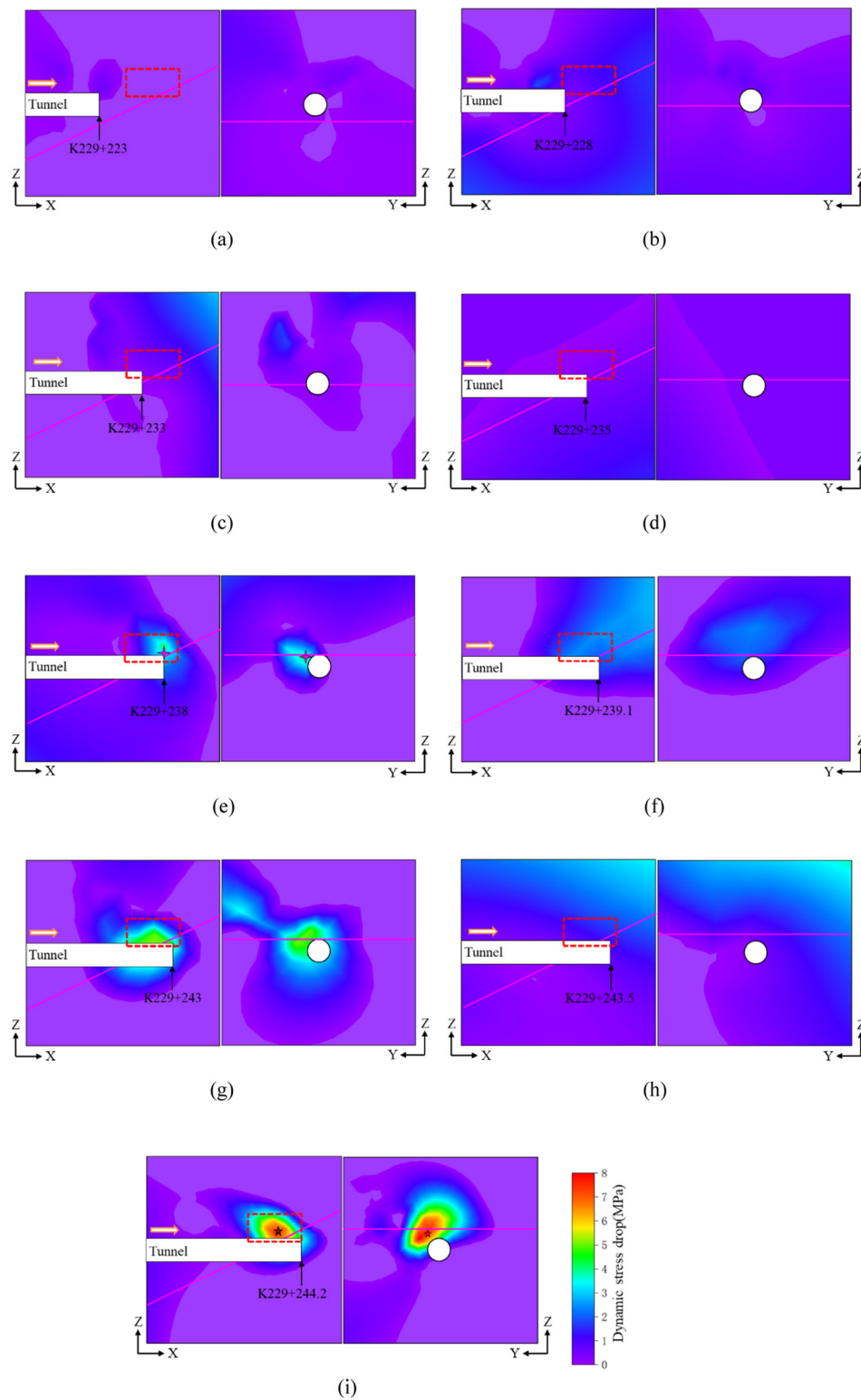

Fig. 15 Evolution of the energy of the MS events during the development process of the fault rockburst

Fig. 16 Evolution of the distribution characteristics of the dynamic stress drop during the fault rockburst. **a** $L = -20 \sim -15$ m. **b** $L = -15 \sim -10$ m. **c** $L = -10 \sim -5$ m. **d** $L = -5$–3 m. **e** $L = -3$–0 m. **f** $L = 0$–1.1 m. **g** $L = 1.1$–5 m. **h** $L = 5$–5.5 m. **i** $L = 5.5$–6.2 m

tensile and shear fracture events were distributed on the left spandrel, and approximately 10–15 m from the tunnel surface. When $L = 1.1$–5.5 m, the proportion of shear fracture events increased, and the high-energy shear fracture events gradually developed to the shallow in the surrounding rock along the fault. When $L = 5.5$–6.2 m, a large number of shear fracture events were concentrated at the left spandrel of the potential rockburst area, and multiple shear fracture events with LgE > 5.0 were distributed along the fault plane.

In addition, the waveform and spectra of the rockburst MS event (18:52:43 on February 15) are analyzed in this case (Figs. 19, 20). When fault rockburst occurred, there was a significant rock fracture signal peak in the range of 10–20 Hz. The evolution of the spectral characteristics of the rock fracture signals collected by the G2 sensor was analyzed during fault rockburst. The result shows that the dominant frequency was 150–250 Hz during the development of fault rockburst, when fault rockburst was about to occur, the dominant frequency gradually decreased. The characteristics of the low-frequency signals were gradually significant, and the proportion was increasing. The dominant frequency decreased to the lowest value when rockburst occurred. The dominant frequencies of the two rockbursts were 41 Hz and 19 Hz, respectively.

The stress–strain curve and failure characteristics of the biotite granite rock sample under the true triaxial state are shown in Fig. 21. The brittleness of this rock is strong, with a strong energy storage capacity, which means more higher intensity of rockburst when rockburst occurs. A macroscopic failure crack is similar to a step, showing tensile and shear fracture, which is consistent with the analysis results based on P-wave development.

The micro-failure modes on the rupture planes of the fault plane were also investigated using scanning electron

microscopy (SEM). Figure 22 shows the SEM scanning results of rock slices on the fault slip plane. The micromorphology of the fracture reflects sliding and rubbing along the crystal plane, which are typical failure modes of shear slip. The local rock powder was formed by the friction of intergranular materials during the fault rockburst. Therefore, this rockburst is a fault rockburst that slipped down along the fault plane.

The above analysis shows that when $L = -3D \sim -2D$, the rock fracture events were mainly tensile fractures and concentrated on the working face. With the excavation, the tensile and shear fracture events occurred together ($L = -2D \sim -1.5D$). When rockburst occurred, the rock fracture events were mainly shear fractures. In addition, partial high-energy tensile and shear fracture events developed from the deep to the surface of the tunnel along the fault, which indicated that the fault plane was gradually penetrating. The high-energy storage capacity of biotite granite provided the basis for the occurrence of the high-intensity rockburst.

4.2 Stress-induced mechanism during the "2021.2.15" fault rockburst based on numerical calculation

To study the stress-induced mechanism, The CASRock (cellular automata software for engineering rock mass fracturing process) [23] was used for numerical calculation. According to the geological conditions exposed by tunnel excavation, a numerical model was established, as shown in Fig. 23. The X-axis represents the excavation direction. The numerical calculation adopts the three-dimensional nonlinear failure criterion for hard rocks [8] and the three-dimensional stress-induced brittle–ductile anisotropic failure model [9]. Through the true triaxial rock mechanics
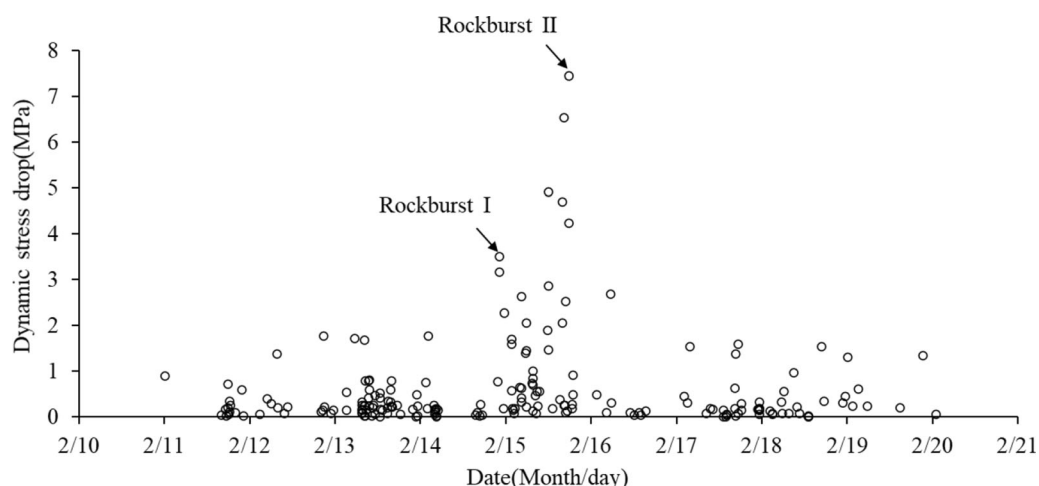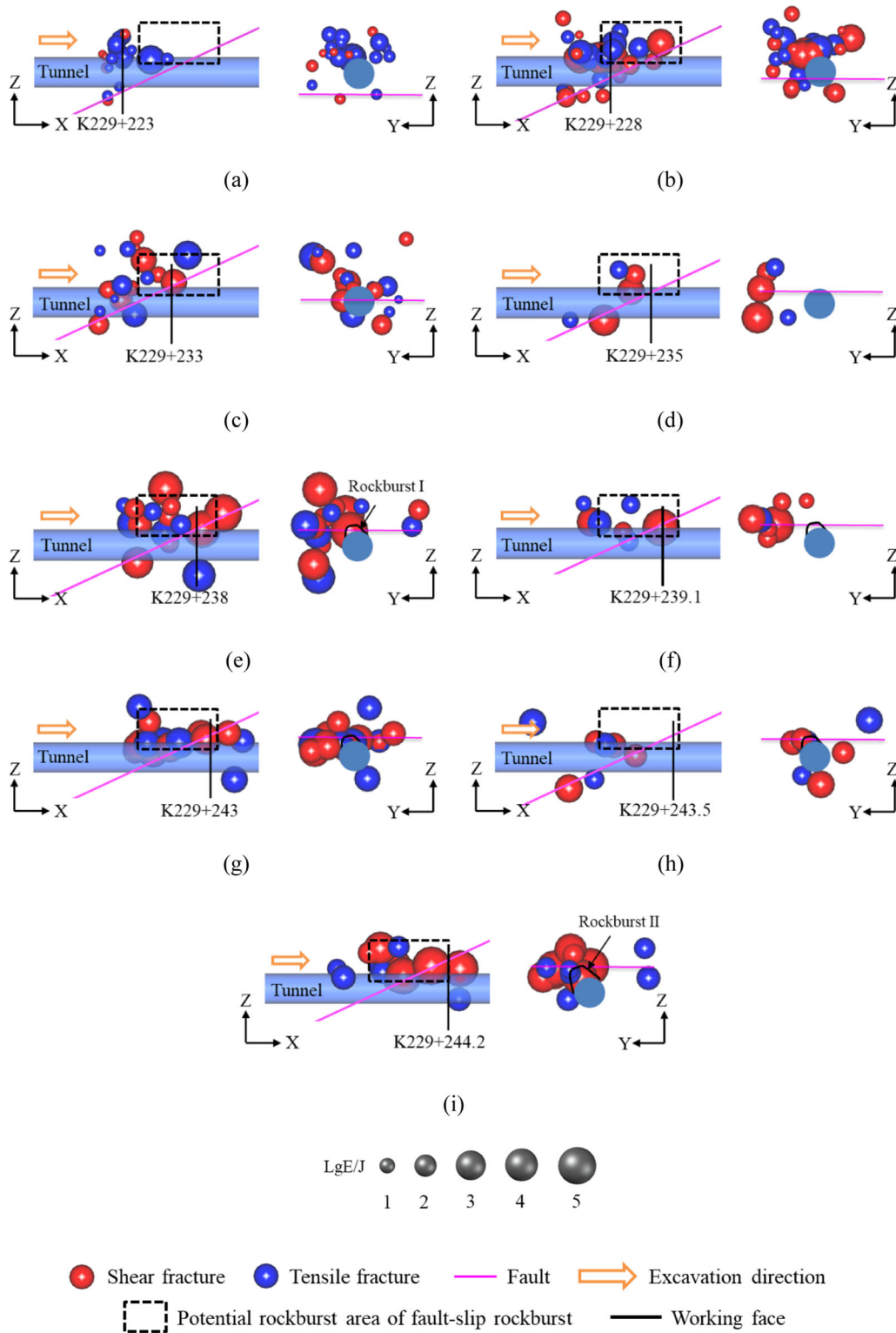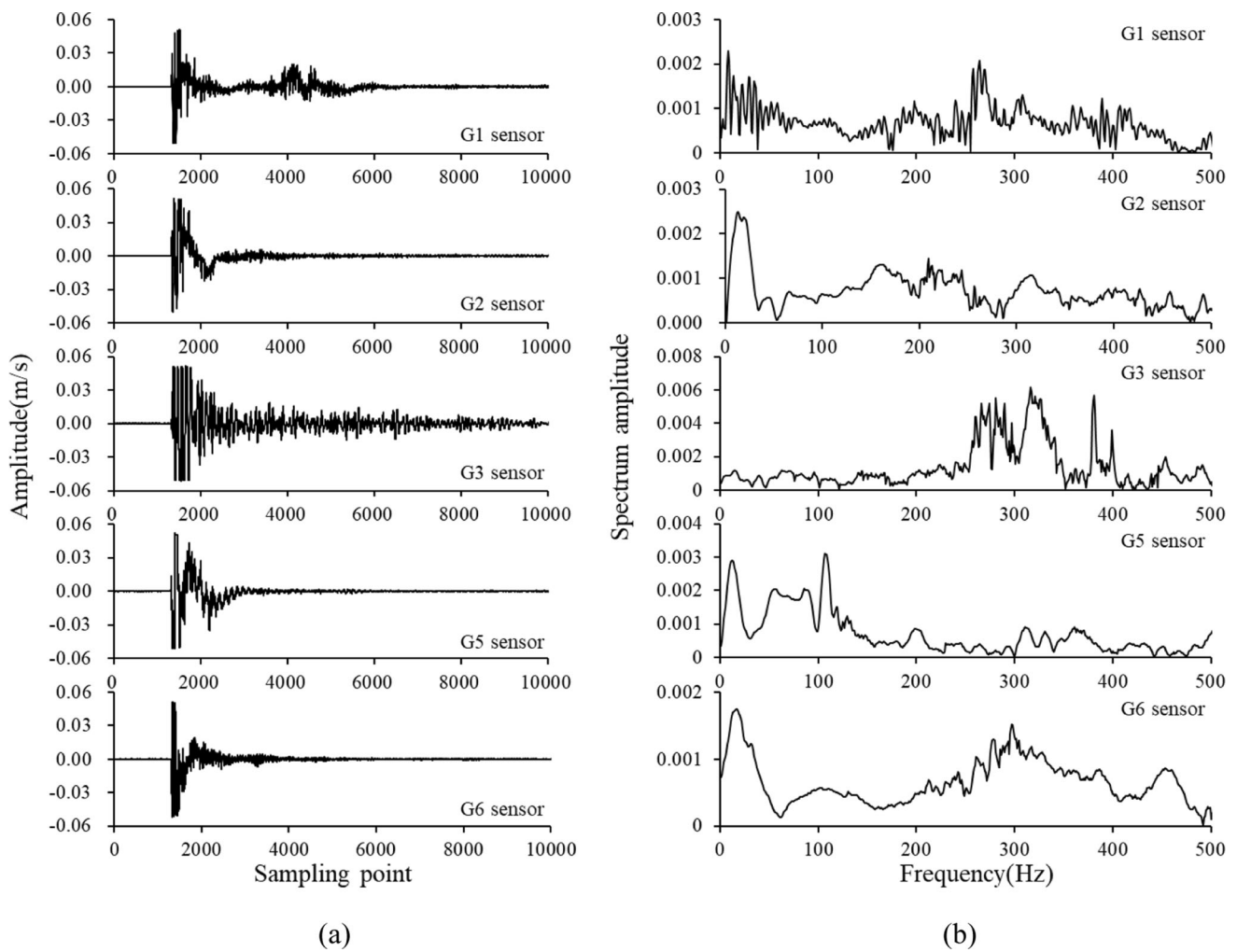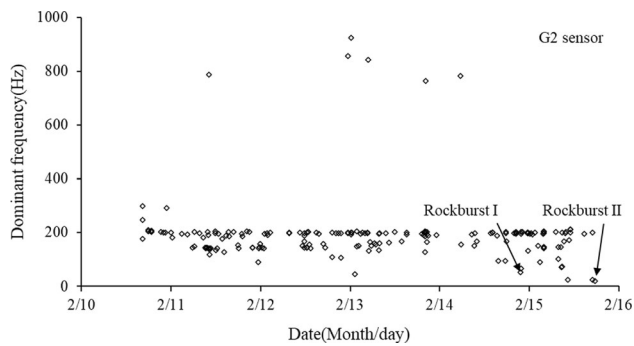

Fig. 17 Evolution of the dynamic stress drop during the fault rockburst

Fig. 18 Evolution and distribution of the rock fracture events during the development of the fault rockburst. **a** $L = -20 \sim -15$ m. **b** $L = -15 \sim -10$ m. **c** $L = -10 \sim -5$ m. **d** $L = -5$–3 m. **e** $L = -3$–0 m. **f** $L = 0$–1.1 m. **g** $L = 1.1$–5 m. **h** $L = 5$–5.5 m. **i** $L = 5.5$–6.2 m

Fig. 19 a The MS waveforms and **b** Frequency spectra of the rockburst event with the greatest MS energy


Fig. 20 The dominant frequency of rock fracture waveforms during the development of the fault rockburst

test, the three-dimensional failure criterion parameters of the rock sample were obtained (Cohesion: c, Friction angle: φ, Material constant: s and t). The mechanical parameters of the rock masses and fault are shown in Table 2. The geostress components (Table 3) were calculated by

coordinate transformation based on the in situ stress measurement results.

Figure 24 shows the maximum principal stress distribution and stress vector distribution of the reference section A, when $L = 6.2$ m. It can be seen that the stress is concentrated in the potential rockburst area, and the greatest value of maximum principal stress is 74.3 MPa. Affected by the fault, the direction of main stresses near the fault deflects, which is obviously different from direction of stress in other areas. The direction of the maximum principal stress in the hanging wall and footwall is approximately horizontal (Y-axis), which provides power for the horizontal slipping of the fault. At the same time, affected by excavation unloading, normal stress of the section was at a low level, which lead to σ_3 decreased. Therefore, normal stress of the fault plane decreased gradually. According to Eqs. (1–3), when $L = -20$–5 m, the dynamic friction factor (μ) of the fault plane was calculated (Fig. 25). Since there was no high-pressure pore water aquifer in the study area, the pore water pressure was
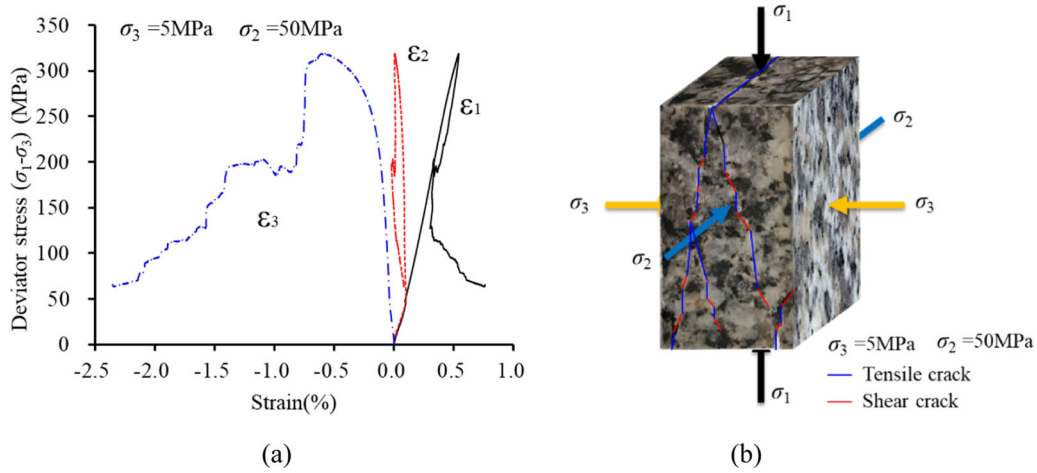
Fig. 21 The stress–strain curve and failure characteristics of biotite granite under true triaxial compression. **a** Complete stress–strain curves. **b** Stress-induced tensile and shear cracking
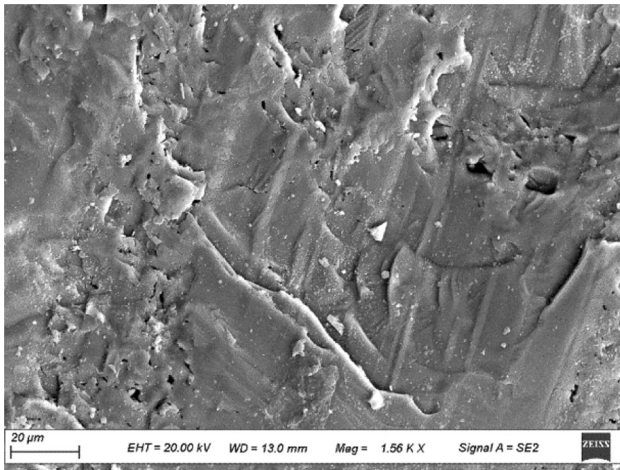
Fig. 22 Scanning electron microscope images used to identify the failure modes in the fracture planes of the fault rockburst

assumed to be hydrostatic pressure, $P_0 = 0.4$ MPa. When $L = -15$ m, μ started to decrease slowly, which means that the fault began to be affected by excavation, and the

shear strength of the fault began to decline. When $L = 0$ m, μ decreased to 0.51, and the fault had slight dislocation. When $L = 6.2$ m, μ further decreased to 0.39, which provided favorable conditions for the horizontal slipping of fault. The above characteristics were also similar to the spatial evolution characteristics of MS activity during the development of the fault rockburst.

$$\sigma' = a^2(\sigma_1 - P_0) + b^2(\sigma_2 - P_0) + c^2(\sigma_3 - P_0) \quad (1)$$

$$\tau = \sqrt{a^2(\sigma_1 - P_0)^2 + b^2(\sigma_2 - P_0)^2 + c^2(\sigma_3 - P_0)^2 - \sigma'^2} \quad (2)$$

$$\mu = \frac{\tau}{\sigma'} \quad (3)$$

where σ' and τ are the normal stress and shear stress on the fault plane. σ_1, σ_2 and σ_3 are the maximum principal stress, intermediate principal stress and minimum principal stress, respectively. a, b and c are the cosines of the angles between the normal direction of the fault plane and each
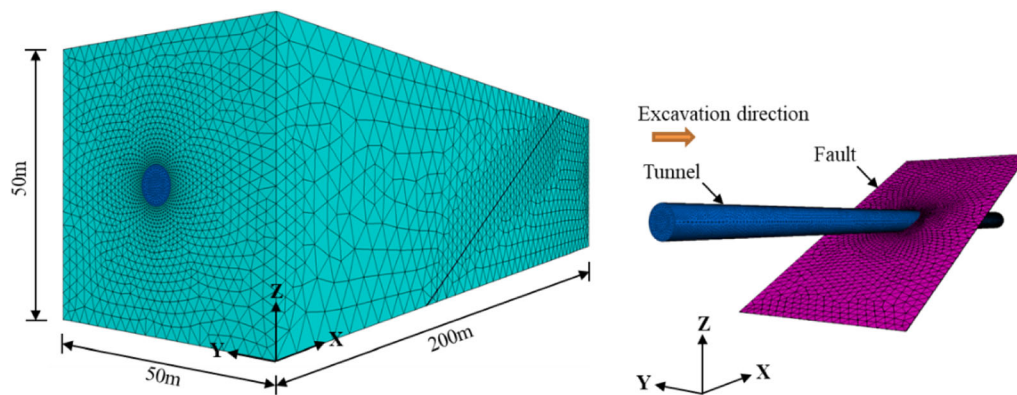
Fig. 23 Numerical model of "2021.2.15" fault rockburst

Table 2 Mechanical parameters used for the rock masses and faults in the CASRock models

Parameter	Value	
	Rock mass	Fault
Friction angle (°)	24.5	15
Cohesion strength (MPa)	15	0.23
Residual friction angle (°)	43	35
Residual cohesion strength (MPa)	2.0	0.035
Tensile strength (MPa)	2.6	0.28
Young's modulus (GPa)	30.2	12.7
Poisson's ratio	0.22	0.25
Density (kg/m³)	2700	1800
Dilation angle (°)	6	5
Strength difference coefficient between generalized triaxial extension and generalized triaxial compression (s)	0.95	0.72
Material constant controlling the maximum strength increasing ratio affected by σ_2 (t)	0.88	0.8

Table 3 Initial geostress state used in the CASRock model

σ_x(MPa)	σ_y(MPa)	σ_z(MPa)	τ_{xy}(MPa)	τ_{yz}(MPa)	τ_{xz}(MPa)
− 16.5	− 32.6	− 21.5	− 1.5	6.4	0.95

stress principal axis, respectively. P_0 is the pore water pressure; and μ is the dynamic friction factor.

4.3 The development mechanism of the "2021.2.15" fault rockburst

According to the case study of "2021.2.15" fault rockburst, the failure characteristics, temporal and spatial evolution of MS activity and rock fracture mechanism were studied. During the development of the fault rockburst, high-energy events occurred near the fault plane in the deep of the surrounding rock and developed along the fault to the shallow of the surrounding rock, forming an energy concentration zone. The crack gradually initiated and extended along the fault plane (Fig. 13). At the same time, the angle between the maximum principal stress and the fault strike was 21–26°, which accelerated the penetration of the fault plane and provided energy for the horizontal slipping of fault. In addition, σ_3 decreased under the influence of excavation unloading, and the normal stress and cohesion of the fault decreased, leading to the decrease of shear strength. At the same time, the fault was more prone to slip under the maximum horizontal principal stress. Therefore, fault slipped under the joint influence of the geological

characteristics, the in situ stress characteristics and the tunnel excavation unloading. Based on the above conclusions, a conceptual model simulating fault rockburst was established, as shown in Fig. 26. In each figure, the left side is the longitudinal section of the tunnel, and the right side is the reference section A.

When $L = -3D \sim -2D$, the rock fracture events are mainly distributed around the tunnel and close to the working face under high stress, and are mainly tensile. Tensile cracks occur near the fault sporadically, and this stage corresponds to the calm stage. When $L = -2D \sim -1.5D$, as the dynamic stress drop increases slowly, tensile and shear cracks begin to occur near the fault plane, and tensile cracks occur sporadically in the deep of the surrounding rock, this stage is the crack initiation stage. When $L = -1.5D \sim -0.5D$, the dynamic stress drop continues to increase, and tensile and shear cracks gradually generate and propagate along fault to the shallow of the surrounding rock, which corresponds to the crack development stage. When $L = -0.5D$–0, the dynamic stress drop near the working face and fault increases rapidly to 3.51 MPa, the energy is concentrated in the shallow of the surrounding rock. Under the excavation and the maximum horizontal principal stress, the fault slips slightly, and some shear cracks extend and penetrate along the fault plane. The energy accumulated in the shallow of the surrounding rock and is released rapidly, causing rockburst I, this stage is the crack accumulation–slight fault dislocation stage. When $L = 0$–0.7D, until rockburst pit I was exposed. The bolt and steel arch support were adopted in time, which effectively improves the bearing capacity of the surrounding rock and provides a basis for further energy accumulation. During tunneling, tensile and shear cracks approximately parallel to the fault plane continue to extend and penetrate. Energy continues to accumulate in potential rockburst area, and the rockburst risk further increases, this stage is the further crack accumulation stage. When $L = 0.7D$–0.9D, under the influence of excavation unloading, σ_3 further decreases. The normal stress of fault is relatively low, and even the cohesion is lost, leading to the reduction of shear strength, the fault is more prone to slip. At the same time, under influence of the maximum horizontal principal stress, the cracks approximately parallel to the fault plane continue to extend rapidly until the fault plane penetrates, which leads to horizontal shear slipping. The elastic energy near the fault is released sharply, resulting in rockburst II, this stage corresponds to the crack penetration–fault slip stage.

In conclusion, during the development process of the fault rockburst, the stress concentration zone is formed at the junction of fault and rock mass, under the maximum horizontal principal stress and excavation unloading, cracks approximately parallel to the fault plane gradually

(a)

(b)
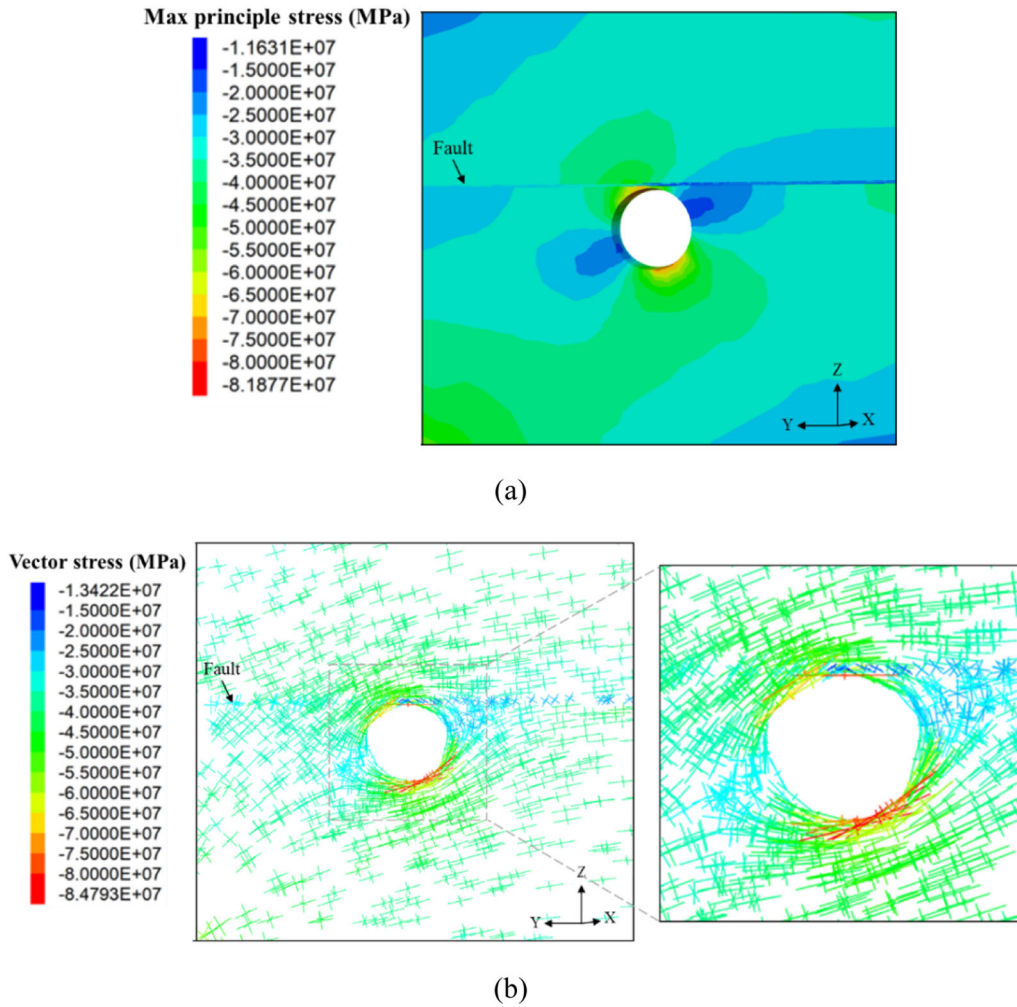
Fig. 24 Numerical simulated stress state during tunnel excavation at reference section A when $L = 6.2$ m. a Maximum principal stress distribution. b Stress vector distribution
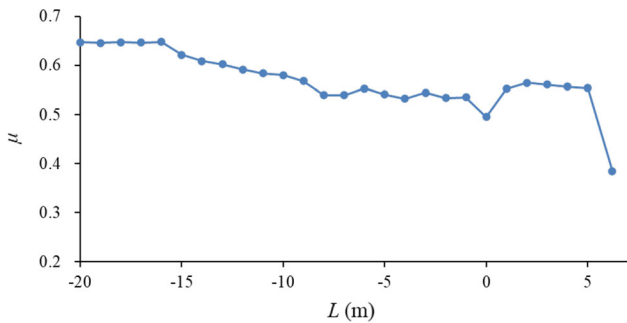

Fig. 25 Evolution of the calculated dynamic friction factor of the fault plane with excavation

occur and extend from deep to shallow of the surrounding rock until they penetrate along the fault plane. Horizontal shear slipping occurs, resulting in a sharp release of elastic energy. Finally, fault rockburst occurred.

5 Discussion

In some previous studies, there is a close relationship between the deformation and failure of a rock mass and the accumulation of deformation on a fault plane, and no rock fracture signal will occur during the occurrence of fault rockburst [27], MS monitoring and other means may be ineffective for fault rockburst monitoring. However, the spectral characteristics of this case show that (Figs. 22, 23), when fault rockburst occurs, the dominant frequency is 19 Hz, with significant low-frequency characteristics. Some studies show that the dominant frequencies of strain rockbursts and strain-structural slip rockbursts are mainly 150–300 Hz [33], MS monitoring system can effectively capture the fracture events within this dominant frequency range. In contrast, when fault rockburst occurs, the dominant frequency is low, and the signal is not easy to capture. Therefore, we should focus on the low-frequency signal capture ability of MS monitoring equipment, and provide
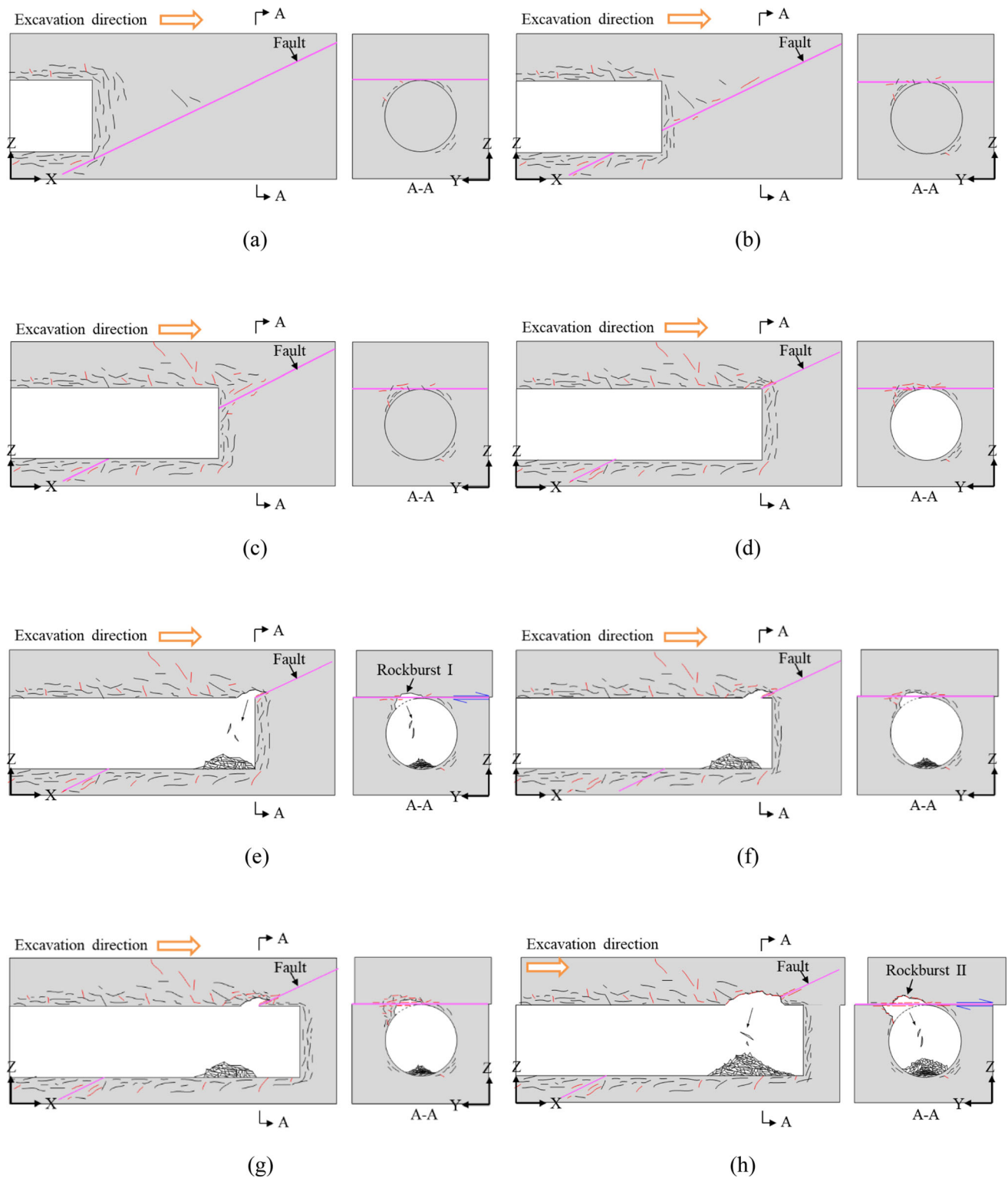
Fig. 26 Conceptual model of the development mechanism of the fault rockburst. **a** Cracks generate sporadically near the fault when the working face is far away from fault. **b** Cracks generate due to stress rise. **c** A large amount cracks generate in the hanging wall due to the rising stress when the working face approaches fault. **d** Cracks extend and penetrate due to the slight dislocation of the fault and the higher stress when the working face is closer to the fault. **e** Rockburst I occurs. **f** A large number of cracks generate continually near the fault due to the excavation and higher stress as the working face gradually moves away from the fault. **g** Cracks penetrate along the fault plane. **h** Cracks extend and penetrate, and finally rockburst II occurs

technical support for capturing fault slip signals. In this case, when rockburst occurs, the dynamic stress drop increases rapidly, some shear fracture events occur near the fault plane, which means that the fault is likely to slip at this time. Dynamic stress drop can be obtained by MS monitoring system; therefore, combined with the characteristics of low dominant frequency before fault rockburst occurs, the above characteristics can be used as one of the evaluation indexes of fault slip. At the same time, combined with other MS information and geological characteristics, the warning method of fault rockburst is established, which will be the focus of future research.

The present research shows that the essence of the development mechanism of the fault rockburst is that the tensile and shear cracks extend and penetrate from deep to shallow of the surrounding rock, which leads to fault slip and intense rockburst. Therefore, it is key to control the crack initiation and propagation in the deep of the surrounding rock near the fault plane timely, which can slow down fault slip. Corresponding measures should be taken to reduce the energy and stress in the deep of the surrounding rock. Crack propagation near the fault is confined by the multiple supports, and it can be controlled in the early stage of rockburst development. At the same time, according to the essence of fault rockburst, fault dislocation can be slowed down or even prevented by shear bolts and other methods to reduce the risk of fault rockburst.

In addition, the development process of the fault rockburst under the D&B and TBM tunneling method is compared, as shown in Fig. 27. The (normalized) time at which the first event occurred in the development process of the fault rockburst is set to 0.0 and the last one to 1.0, and the fault rockburst occurred at 1.0 (normalized time). Affected by the strong disturbance of D&B, when the working face just exceeds 1 m of fault after the completion of construction cycle, fault rockburst occurs, the energy release rate reaches 97.8%, the energy of rockburst I is higher than rockburst II [39]. In comparison, the disturbance of TBM is weak, fault rockburst occurs when the working face exceeds more than 6 m from the fault, and the energy release rate is only 63.2%, and the energy of rockburst II is higher than rockburst I. Although the development process of the fault rockburst under different excavation methods is relatively similar, there are some differences when the fault rockburst occurs. The energy release is slow in TBM excavation due to its weak disturbance to surrounding rock. The low intensity rockburst occurs before the high-intensity main rockburst. For example, in the case of "2021.2.15" fault rockburst, the low intensity rockburst I occurred before the intensity rockburst II. Therefore, based on the above characteristics, targeted warning and mitigation methods of fault rockburst can be proposed accordingly according to different excavation methods.
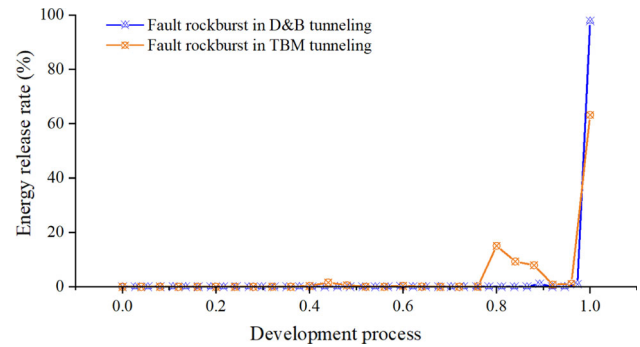

Fig. 27 Development process of the fault rockburst under different excavation methods

6 Conclusion

In this work, an intense fault rockburst in a deep TBM tunnel in China was introduced. The failure characteristics of fault rockburst were analyzed, the temporal and spatial evolution of the MS activity, dynamic stress drop and spatial distribution characteristics of the fracture mechanism were studied. Finally, the development mechanism of fault rockburst was revealed.

The MS monitoring system successfully recorded the whole development and occurrence process of the fault rockburst. The temporal and spatial evolution of MS activity shows that low-energy events first occur near the fault during the development of the fault rockburst. The high-energy events occur in the deep of the surrounding rock and develop to the shallow along the fault. When rockburst occurs, the energy is released in the shallow of surrounding rock. The MS energy is released intermittently during the rockburst development The analysis shows that the occurrence process of the "2021.2.15" fault rockburst experienced six stages: calm stage, crack initiation stage, crack development stage, crack accumulation–slight fault dislocation stage, further crack accumulation stage and crack propagation–fault slip stage. Significantly, when the working face is approximately double the tunnel diameter from the fault, the fault begins to be affected. At the same time, the dynamic stress drop is also consistent with the above laws during the development of rockburst.

In addition, the failure mechanism is analyzed during the development process of fault rockburst. Tensile and shear fractures occur together during the development process of fault rockburst, when rockburst occurs, the rock fracture events are mainly shear fractures. Biotite granite with high brittleness provides the basis for high-intensity rockburst. Numerical results show that the normal stress of the fault plane gradually decreases during excavation, which makes the fault more prone to slip. Then, based on the above conclusions, a conceptual model simulating fault rockburst is established. During the development process

of the fault rockburst, the interface between fault and rock mass establishes the basic conditions for stress concentration. The maximum horizontal principal stress approximately parallel to the fault plane provides the energy for the horizontal shear slipping, and excavation-induced stress unloading becomes an auxiliary factor for the horizontal slipping of fault. The above factors accelerate the propagation of cracks along the fault plane, resulting in horizontal shear slipping and inducing fault rockburst. Finally, targeted warning and mitigation measures can be proposed, based on different excavation methods.

Data availability The datasets generated during and analyzed during the current study are available from the corresponding author on reasonable request.

Declarations

Conflict of interest The authors declare that they have no known competing financial interests or personal relationships that could have appeared to influence the work reported in this paper.

References

1. Alavi Nezhad Khalil Abad SV, Mohamad ET, Komoo I, Kalatehjari R (2014) A typical weathering profile of granitic rock in Johor, Malaysia based on joint characterization. Arab J Geosci 8:2191–2201
2. Brace WF, Byerlee JD (1966) Stick-slip as a mechanism for earthquakes. Science 153:990–992
3. Chen BR, Feng XT, Fu QQ, Wang B, Zhu XH, Li T, Lu CP, Xia H (2020) Integration and high precision intelligence microseismic monitoring technology and its application in deep rock engineering. Rock Soil Mech 41:2422–2431
4. Cheng L, Zhou K, Li JL (2018) Experimental investigation on physical and mechanical properties of altered granite. Nonferrous Metals Eng
5. Durrheim R, Haile A, Roberts M, Schweitzer J, Spottiswoode S, Klokow J (1998) Violent failure of a remnant in a deep South African gold mine. Tectonophysics 289:116
6. Feng GL, Feng XT, Chen BR, Xiao YX, Jiang Q (2015) Sectional velocity model for microseismic source location in tunnels. Tunn Undergr Space Technol 45:73–83
7. Feng GL, Feng XT, Chen BR, Xiao YX, Yu Y (2015) A microseismic method for dynamic warning of rockburst development processes in tunnels. Rock Mech Rock Eng 48:2061–2076
8. Feng XT, Kong R, Yang CX, Zhang XW, Wang ZF, Han Q, Wang G (2020) A three-dimensional failure criterion for hard rocks under true triaxial compression. Rock Mech Rock Eng 53:103–111
9. Feng XT, Wang ZF, Zhou YY, Yang CX, Pan PZ, Kong R (2021) Modelling three-dimensional stress-dependent failure of hard rocks. Acta Geotech 16:1647–1677
10. Hu L, Feng XT, Xiao YX, Wang R, Feng GL, Yao ZB, Niu WJ, Zhang W (2020) Effects of structural planes on rockburst position with respect to tunnel cross-sections: a case study involving a railway tunnel in China. Bull Eng Geol Environ 79:1061–1081
11. Jerzy B (2012) Rockburst hazard and the fight for its alleviation in South African gold mines : Salamon, M D G In: Rockbursts: Prediction and Control (papers to the Symposium, London, 20 October 1983) P11–36. Publ London: IMM, 1983. Int J Rock Mech Min Sci Geo Abs 21: 168–178
12. Jiang LS, Kong P, Zhang PP, Shu JM, Wang QB, Chen LJ, Wu QL (2020) Dynamic analysis of the rock burst potential of a longwall panel intersecting with a fault. Rock Mech Rock Eng 53:1737–1754
13. Kato N, Satoh T, Lei X, Yamamoto K, Hirasawa T (1999) Effect of fault bend on the rupture propagation process of stick-slip. Tectonophysics 310:81–99
14. Li J, Wang MY, Li XP, Huang HX, Jiang HM (2018) The mechanics mechanism and occurrence conditions of sliding type rockbursts triggered by weak disturbance. Chin J Rock Mech Eng 37:3205–3214
15. Lu CP, Liu B, Liu B, Liu Y, Wang HY, Zhang H (2019) Anatomy of mining-induced fault slip and a triggered rockburst. Bull Eng Geol Environ 78:5147–5160
16. Lu CP, Liu GJ, Liu Y, Zhang H (2019) Mechanisms of rockburst triggered by slip and fracture of coal–parting–coal structure discontinuities. Rock Mech Rock Eng 52:3279–3292
17. Lu CP, Liu Y, Zhang N, Zhao TB, Wang HY (2018) In-situ and experimental investigations of rockburst precursor and prevention induced by fault slip. Int J Rock Mech Min Sci 108:86–95
18. McLaskey GC, Lockner DA (2016) Calibrated Acoustic emission system records M 3.5 to M 8 events generated on a saw-cut granite sample. Rock Mech Rock Eng 49:1–10
19. Nemat-Nasser S, Horii H (1983) Rock failure in compression. Int J Eng Sci 22:999–1011
20. Niu WJ, Feng XT, Feng GL, Xiao YX, Yao ZB, Zhang W, Hu L (2022) Selection and characterization of microseismic information about rock mass failure for rockburst warning in a deep tunnel. Eng Fail Anal 131:105910
21. Ohnaka M, Kuwahara Y, Yamamoto K (1987) Constitutive relations between dynamic physical parameters near a tip of the propagating slip zone during stick-slip shear failure. Tectonophysics 144:109–125
22. Ortlepp WD (2000) Observation of mining-induced faults in an intact rock mass at depth. Int J Rock Mech Min Sci 37:423–436
23. Pan PZ, Feng XT, Hudson JA (2009) Study of failure and scale effects in rocks under uniaxial compression using 3D cellular automata. Int J Rock Mech Min Sci 46:674–685
24. Paul G, Okubo J, H, Dieterich, (1984) Effects of physical fault properties on frictional instabilities produced on simulated faults. J Geophys Res 89:5817–5827
25. Ruff LJ (1999) Dynamic stress drop of recent earthquakes: variations within subduction zones. Birkhäuser, Basel
26. Ryder JA (1988) Excess shear stress in the assessment of geologically hazardous situations. J S Afr I Min Metall 88:27–39
27. Salamon M (1970) Stability, instability and design of pillar workings. Int J Rock Mech Min Sci Geo Abs 7:613–631
28. Savage JC, Lockner DA, Byerlee JD (1996) Failure in laboratory fault models in triaxial tests. J Geophys Res Solid Earth 101:22215–22224
29. Shi JW, Chen ZL (2014) Based on numerical simulation study of rockburst in roadway induced by fault. Adv Mater Res 962–965:370–374
30. Song YM, Ma SP, Yang XB, Jiang YD (2011) Experimental investigation on instablty transient process of fault rockburst. Chin J Rock Mech Eng 30:812–817

31. Williams TJ, Wideman CJ, Scott DF (1992) Case history of a slip-type rockburst. Pure and Appl Geophys 139:627–637

32. Wu J, Zhang XY, Yu LY, Zhang LW, Wu T (2022) Rockburst mechanism of rock mass with structural planes in underground chamber excavation. Eng Fail Anal 139:106501

33. Xiao YX, Feng XT, Chen BR (2015) Evolution of frequency spectrum during instant rockbursts in deep inoculation tunnel. Rock Soil Mech

34. Xiao YX, Feng XT, Chen BR, Feng GL (2015) Evolution of frequency spectrum during instant rockbursts in deep inoculation tunnel. Rock Soil Mech

35. Xiao YX, Feng XT, Chen BR, Feng GL, Yao ZB, Hu LX (2017) Excavation-induced microseismicity in the columnar jointed basalt of an underground hydropower station. Int J Rock Mech Min Sci 97:S1365160917304665

36. Zhang CQ, Feng XT, Zhou H, Qiu SL, Wu WP (2012) Case histories of four extremely intense rockbursts in deep tunnels. Rock Mech Rock Eng 45:275–288

37. Zhang W, Feng XT, Bi X, Yao ZB, Xiao YX, Hu L, Niu WJ, Feng GL (2021) An arrival time picker for microseismic rock fracturing waveforms and its quality control for automatic localization in tunnels. Comput Geotech 135:104175

38. Zhang W, Feng XT, Xiao YX, Feng GL, Yao ZB, Hu L, Niu WJ (2020) A rockburst intensity criterion based on the Geological Strength Index, experiences learned from a deep tunnel. Bull Eng Geol Environ 79:3585–3603

39. Zhang W, Feng XT, Yao ZB, Hu L, Xiao YX, Feng GL, Niu WJ, Zhang Y (2022) Development and occurrence mechanisms of fault-slip rockburst in a deep tunnel excavated by drilling and blasting: a case study. Rock Mech Rock Eng 55:5599–5618

40. Zhao ZN, Feng XT, Chen BR, Feng GL, Chen TY (2013) Study of relativity between rockburst and microseismic activity zone in deep tunnel. Rock Soil Mech 34:491–497